Computer vision AC-STEM automated image analysis for 2D nanopore applications

*Joshua Chen[1,2], Adrian Balan[3], Paul Masih Das[1], Jothi Priyanka Thiruraman[1,4], Marija Drndić[1]**

[1] Department of Physics and Astronomy, [2] Department of Materials Science and Engineering,

University of Pennsylvania, Philadelphia, Pennsylvania, 19104, USA

[3] AI Insights SAS, Paris 75015, France

[4] Department of Electrical and Systems Engineering,

University of Pennsylvania, Philadelphia, Pennsylvania, 19104, USA

*Corresponding author: drndic@physics.upenn.edu.

ABSTRACT:

Transmission electron microscopy (TEM) has led to important discoveries in atomic imaging and as an atom-by-atom fabrication tool. Using electron beams, atomic structures can be patterned, annealed and crystallized, and nanopores can be drilled in thin membranes. We review current progress in TEM analysis and implement a computer vision nanopore-detection algorithm that achieves a 96% pixelwise precision in TEM images of nanopores in 2D membranes (WS_2), and discuss parameter optimization including a variation on the traditional grid search and gradient ascent. Such nanopores have applications in ion detection, water filtration, and DNA sequencing, where ionic conductance through the pore should be concordant with its TEM-measured size. Standard computer vision methods have their advantages as they are intuitive and do not require extensive training data. For completeness, we briefly comment on related machine learning for 2D materials analysis and discuss relevant progress in these fields. Image analysis alongside TEM allows correlated fabrication and analysis done simultaneously *in situ* to engineer devices at the atomic scale.

Keywords: TEM, transition metal dichalcogenide, 2D nanopores, ion transport, computer vision, OpenCV

1. INTRODUCTION:

Microscopy methods have become increasingly refined as materials and devices reach smaller scales. Transmission electron microscopy (TEM) provides insights into the structure, properties, and interactions of materials down to ~ 40 pm resolution[1]. Specifically, low-dimensional materials are projected to be the future of electronic and optical technology. For example, 2D spintronics may provide electronics beyond Moore's law,[2] and 2D materials-based radio frequency wireless communication systems have been advocated as platforms for Internet-of-things applications[3].

In TEM, the combination of spatial, time, and energy resolution allows for high quality insight into the morphology, chemistry, and electronic structure of materials[4]. Developments have spanned observations on the distribution of dopants[5] and defects[6] in graphene, in situ imaging of VO_2 phase transformations[7], structural shifts during material growth[8,9], atomic surface diffusion in Pt nanoparticles[10], distinction of phases in nanoparticles[11], and more. TEM has been studied for fabrication[12–19], including patterning, annealing and crystallization to make 2D nanopores, nanoribbons, and nanopore-nanoribbon field-effect-transistor devices. Electron-beam gating has been demonstrated to realize *in situ* 2D MoS_2 field-effect transistors[20], towards building materials atom-by-atom. Though TEM-based fabrication may be replaced for some applications with lower cost methods (for example making pores by acid-etching[21] and electroporation[22] *vs*. irradiation[23]), *in situ* TEM allows atomic precision, where observation, fabrication, and analysis can happen simultaneously. Automated image analysis is important to achieve this goal, as opposed to manual image processing one-by-one—given a single mm^2 2D material sample, 1.6 billion TEM images of area 25 nm x 25 nm are required to image the mm^2 area.

In this paper, we overview computer algorithms to automate TEM image analysis (*Section 1.3)* and focus on computer vision which has been researched as early as the 1980s[24]. Standard computer vision methods using pre-built functions are favorable when knowledge about specific features in the image are incorporated into the feature recognition algorithm and/or the problem is not particularly complicated. We present new aberration-corrected scanning transmission electron microscope (AC-STEM) images of nanoporous 2D monolayer WS_2, created by ion irradiation. We overview the 2D materials growth, transfer of 2D flakes onto TEM-suitable devices, nanopore fabrication, followed by TEM imaging and analysis through standard computer vision methods. We review the relevant background and applications for these 2D pores, nanodevice fabrication methods, and image analysis techniques. Image analysis is performed using standard computer vision and we discuss two methods to optimize algorithm parameters: a variation on a traditional grid search with a visual component and a gradient descent implementation (gradient ascent). For completeness, we briefly address a deep learning application.

1.1 Background on 2D transition metal dichalcogenides and 2D nanopore devices

Two-dimensional transition metal dichalcogenides (TMDs) like MoS_2 and WS_2 have garnered attention for microelectronics, batteries, solar cells, sensors, and biomedicine.[25] They share some aspects with graphene[26], combining atomic thickness, a direct band gap, strong spin-orbit coupling, and robustness[27], and present interesting properties as atomically-thin membranes[28]. 2D TMDs offer the possibility to fabricate holes for applications from water filtration and desalination[29,30] to DNA/protein sequencing[31] and molecular sensing. A summary of 2D pores[32] is in Refs. 30 and 33[30,33]. Sub-nanometer vacancies in 2D materials have been created, for example with electron-beam irradiation[34–38], ion irradiation[23,39–41], oxygen plasma[42], and chemical etching[21,43], where ion-irradiated 2D membranes can have ~ 10,000 to 70,000 pores/μm^2 with an average diameter of ~ 0.5 nm [40] (**Figure 1**). Sub-nanometer vacancies have applications in fluid filtration as they are comparable to the size of water molecules (~ 0.3

nm) and hydrated ions (~ 1 nm)[29]. Other applications include molecular analysis and osmotic power generation[44], and atomic vacancies can serve for efficient water-desalination because water transport scales inversely with membrane thickness[45–47].2D material pores have also been investigated for DNA sequencing[33,48–54], as have protein pores[55–58]. MoS_2 has shown particular promise, similar to graphene [48–50], since its atomic thickness (~ 0.6-1.7 nm[49,51,59]) approaches the inter-nucleotide distance of DNA [45,60,61]. Other 2D pores[29,33] include WS_2[53], boron nitride[52,62], MXenes[54] and phosphorene[63,64]. Single "zero D" MoS_2 pores (with ~ 1-5 missing Mo atoms) show current-voltage characteristics[59,65,66] that depart from those of larger pores[67,68]. TMD pores have shown better wetting than graphene and have a predicted higher water flux, specifically for pores with Mo-terminated edges[45].

1.2 Emerging nanoscale device fabrication methods in TEM for ex situ applications.

TEMs have been optimized for characterization and imaging[69]. Electron irradiation "damage", required for nanopore drilling, had previously been considered a nuisance, with exceptions from the 1970s onwards[70] (other references are in Ref. 12[12]). With the advancements of device physics, however, there has been pressure to modify TEMs into fabrication tools towards "transmission electron beam ablation lithography"[12] at the atomic scale[14,71]. Patterning holes/pores and nanowires/nanoribbons/nanochannels, moving single atoms, materials' annealing/crystallization, are examples now happening in this "TEM-device fabrication" subfield. For example, *in situ* TEM Joule heating by running a current through 2D graphene and MoS_2 nanoribbons can heal defects, clean the 2D surface, bond monolayers, and increase conductance[15,17,35,35,72]. Above some irradiation dose, imaging can degrade the device conductance by creating defects (such as S vacancies in MoS_2)[16,35,73], so TEM fabrication has to be adapted[16]. The TEM beam can be used as a gate for 2D material transistors[20] and " *operando*" TEM [74].

TEMs will likely be automated with real-time data analysis and feedback. As of now, TEMs are unique tools for fabricating pores[29,65] . Electroporation[75] may offer similar possibilities, but TEM remains a "gold standard" for structure characterization and atomic-scale insights in vacuum and other environments[76]. Given that devices can now contain well-characterized atom-sized holes, the field of nanofluidics is merging with electron microscopy, where atomic defects have been studied for decades. Controlled electron irradiation (with electron dose and time that depend on material composition and thickness)[63,64] has been used to drill holes and sculpt sub-10 nm parts[12,13]. Some materials allow easy drilling, while others crystallize for the same parameters[12]. TEM fabrication has been combined with other steps, for example in nanopore-nanoribbon[16,73,77–81] field-effect-transistors (FET) and the nanopore-nanogap devices[12,82–86]. Atomic structures have been made such as carbon atomic chains[87], yet the majority them were not completed into *ex situ* devices. The challenges of electrical contacts are sometimes downplayed[88] and device stability outside of vacuum has to be addressed. It is possible to use the *same* devices for correlated *in situ* and *ex situ* TEM and device characterization, as exemplified by nanopores. 2D membranes are suspended on TEM carbon grids and silicon nitride (SiN) windows. For nanofluidics, the membrane seals the carbon/SiN hole (done by annealing)[16,48]. Requirements are more stringent than with either of the techniques alone.

1.3 TEM image analysis approaches

TEM is generating more data than ever before with a rising number of new materials, requiring image analysis methods for both post-experiment and real time computation to keep up. An experiment can create hundreds of thousands of images in the form of movies, ptychography, and multi-dimensional

series due to the development of new high-speed detectors[89] and the environmental TEM[90]. It is possible to observe dynamic atomic interactions in high resolution over time, providing insight into material processes[91]. Unautomated analysis methods include image analysis programs such as ImageJ[31], in which filter parameters are adjusted according to each image, and images are often processed one-by-one to identify atomic defects, measure distances and angles, and calculate nanopore area[40]. Automation is not a possibility here since parameters require manual tuning. New computational methods must be developed to analyze TEM images autonomously, whether it be identifying nanopores or defects, characterizing them, or other more complicated analyses.[92,93]

Multiple approaches can be taken for image analysis and feature recognition, and the choices can be application dependent. Computer vision[24,94] is a vastly studied field separate from physics imaging, and countless algorithms have been developed for a variety of applications each with their own trade-offs in terms of speed, accuracy, and resource requirements. In the realm of TEM atomic-resolution image analysis of nanomaterials, existing methods have varied across a few main categories. Real space approaches involve detecting deviations in intensity in real space and have been widely studied. As early as 1992, Zuo *et al.*[95] extrapolated lattice templates using a group of atomic columns in simulated high-resolution TEM images and compared intensity peaks to deduce lattice displacements and, thus, mechanical strain. The peak pairs approach, developed by Galido *et al.* [96] in 2007, measured the local shifts of image details around a crystal defect with respect to the ideal, defect-free positions in the bulk. Similarly, Bierwolf *et al.* (2013)[97] identified local displacements by superimposing lattices and analyzing the resultant moiré structures. Kramberger *et al.* (2017)[98] addressed defects subject to beam driven dynamics and implemented a maximum likelihood algorithm to represent graphene samples' intrinsic defect populations. On the contrary to real space approaches, Fourier space approaches have also shown success. Hÿtch *et al.* (2018)[90] employed geometric phase analysis, a technique analyzing peaks in intensity using fast Fourier transform algorithms, to measure and map displacement and strain fields in high-resolution TEM micrographs. Maksov *et al.* (2019)[102] used a Fourier filter and thresholding to segment pores from lattice in WS_2 to create training data for deep learning.

The rise of machine learning has resulted in a variety of new approaches pertaining to TEM atomic -resolution image analysis. Whereas real and Fourier space algorithms use standard programming methods where code is written to address the task head on, machine learning focuses on computer algorithms that improve automatically through experience. One such machine learning method, convolutional neural networks (CNN), has shown promise in image analysis. CNNs are a good fit for image applications implicitly because they are inspired by the structure of the optical neurons in the human eye [99, 100]. Kernels in different layers of the CNN adapt to learn features in an image of different sizes (*i.e.*, number of pixels), with first layers detecting simple image features (lines/dots) and subsequent layers detecting more complex features containing the features detected in the preceding layers. Convolutional neural networks have been used in image segmentation of gold nanoparticles[101] (2020), single particles in cryo-EM images[102] (2017), WS_2 degradation videos[103] (2019), defected graphene as well as metallic nanoparticles[90], and chemical identification and local tracking of transformations[104] (2017). Furthermore, convolutional neural networks have been combined with other methods such as a cascade object detector and local image analysis methods to best identify defects of metal alloys under irradiation[100] (2018).

Image analysis algorithms have become increasingly complicated over time, largely due to the acceleration of machine learning. While machine learning shows great promise, there are its issues. The indirect nature of machine learning can result in the misinterpretation of results and poor reproducibility when done without proper error analysis[105,106], and there exists the danger of overfitting in deep learning applications in which a model is created to fit training data, and not much more[107]. Machine learning

parameters do not often map intuitively to physical features[108], making error analysis and troubleshooting difficult. Thus, it is useful to take a step back from complicated algorithms and revisit standard computer vision solutions that perform simply and reliably, and then compare and combine them with machine learning. OpenCV is an open source computer vision library[109] first released in 2000 that has pre-written functions. Using OpenCV, we investigate direct automated feature recognition and introduce a visual grid search method coined Comprehensive Variable Visual Plotting (CVVP) to address parameter optimization. We compare this method with an optimized algorithm known as a gradient descent (ascent) for parameter optimization and briefly comment on deep learning.

2. METHODS:

2.1 Terminology

In this paper, by "TEM" imaging we refer to all imaging performed inside of a transmission electron microscope (TEM) *machine*. This includes imaging in TEM machines with various resolution capabilities and instrument models, from older TEMs, to high-resolution TEMs (HR-TEM), to more recent aberration-corrected TEMs (AC-TEM) that resolves individual atoms and encompasses different imaging modes including scanning TEM (STEM). We note that images of 2D materials discussed in our work come from "AC-STEM" imaging, taken in the scanning imaging mode and with resolution of 0.1 nm. OpenCV refers to the open source computer vision library used to develop the nanopore-recognition algorithm, and CVVP refers to comprehensive variable visual plotting, a method developed here to mimic a grid search that optimizes our algorithm parameters.

2.2 TMD growth, transfer, and TEM imaging

2D TMDs presented in this work were grown by chemical vapor deposition (CVD) on silicon oxide substrates and then transferred using a KOH-based wet transfer with PMMA resist onto holey TEM carbon grids. All experimental details are as described for samples in Refs. 23 and 40.[23,40] To make pores in 2D membranes, samples were irradiated with 30 kV Ga^+ ion irradiation with doses of either 5.1×10^{13} ions/cm^2 or 6.4×10^{14} ions/cm^2, as in Ref. 23[23]. AC-STEM images were acquired with a JEOL JEM-ARM200CF S/TEM at the Center for Advanced Materials and Nanotechnology at Lehigh University, with resolution of ~ 0.1 nm. At a camera length of 10 cm, either a high-angle annular dark-field (HAADF) detector with a collection angle of 54 - 220 mrad or a bright-field (BF) detector with a collection angle of 0-3 mrad was used.To minimize defect production and expansion of existing defects under the electron beam, an acceleration voltage of 80 kV and probe current of below 20 pA were utilized. This resulted in an imaging exposure dose of ~ 10^6 e^-/nm^2, which is not expected to cause significant knock-on or radiolysis damage[34,35] in monolayer TMDs. Some images were also obtained on a JEOL NEOARM S/TEM with similar beam conditions at the University of Pennsylvania's Singh Center for Nanotechnology.

2.3 Automated image analysis via OpenCV

Figure 1 describes the full process from synthesis of the 2D nanomaterial through chemical vapor deposition to image analysis and the identification of resulting nanopores. The included example TEM image exhibits a 24 nm x 24 nm portion of a 2D WS_2 sample exposed to focused ion-beam (FIB) Ga^+ irradiation with dosage of 5.1×10^{13} ions/cm^2. Given TEM images of WS_2 with nanopores dispersed in ion-irradiated 2D membranes, a straightforward method to automatically identify nanopores from a 2D sheet

is through standard computer vision techniques through OpenCV that focus on extracting features as a human would. The right portion of **Figure 1** indicates the progression of functions to separate dark regions that look like holes ("nanopores") from the rest of the image. In order, the set of steps are: a) a normalizing CLAHE (contrast limited adaptive histogram equalization) function[110], b) an original averaging thresholding function, and c) a final find-contours and minimum area qualifying function, which we call "Selection".

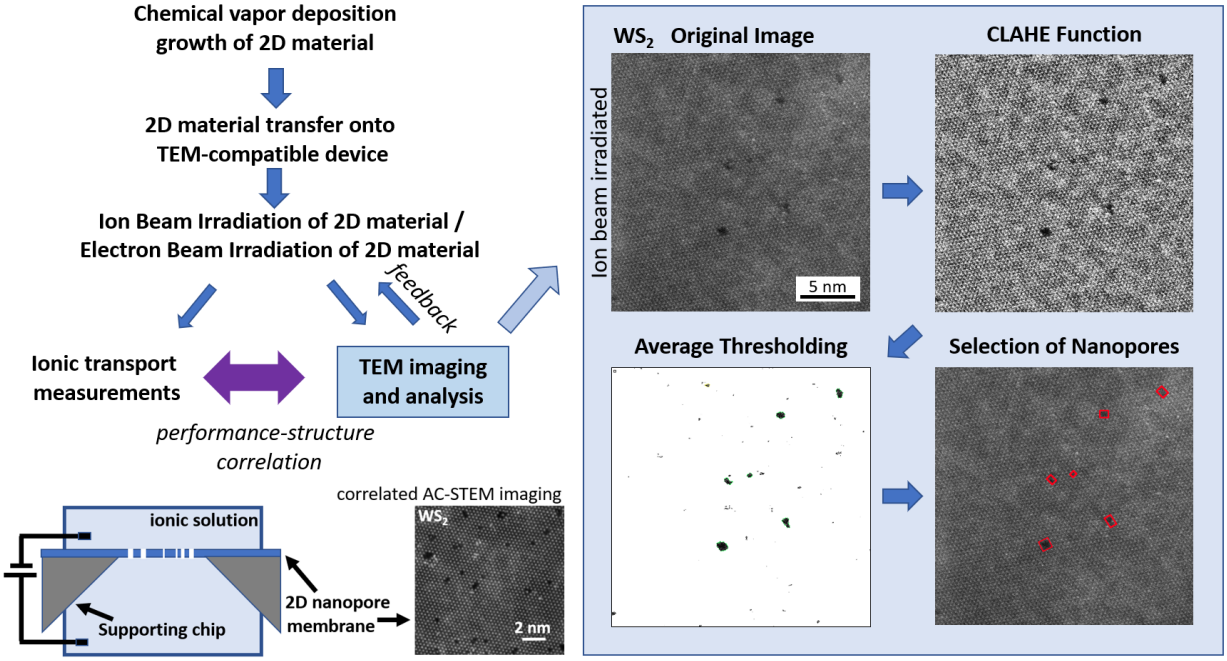

Figure 1. Complete process from 2D material synthesis, to irradiation, to creating nanopores and imaging. The schematic in the bottom left shows a side cross-section view of the ionic transport measurement set-up, where ionic transport (ionic current magnitude measured) should be concordant with inferences from image analysis. The sequence of functions applied to a sample TEM image consists of a normalizing CLAHE function (to equalize for variance in brightness across the image), an Average Thresholding function to separate darker spots from the image, and a final Selection function that specifies which spots qualify as nanopores.

Below, note the bolded terms are parameters that are eventually optimized. The CLAHE function was selected to equalize all portions of each image for brightness. Due to the presence of oxidation/dirt[35] on the sample and other uncontrolled factors that can cause one area of an image to be brighter than another (due to the sample preparation, for example using a PMMA resist and wet transfer[65], and/or TEM imaging conditions), identifying nanopores without the CLAHE function first applied causes uneven recognition across the image, where nanopores are indicated more readily on one portion than another. The CLAHE function segments each image into tiles of controllable ***grid*** size and normalizes each portion independently, effectively judging and evaluating each potential nanopore relative to its surrounding region as a human eye would. The result is a contrast-enhanced image that removes any shadows or uneven brightness. The average thresholding function extracts areas of each image that are sufficiently saturated with darker pixels and identifies those as potential nanopores. Most specifically, the function iterates through each pixel within each TEM image and averages the brightness of surrounding pixels in a specific ***radius*** from it. Pixels with an average brightness greater than a chosen ***threshold*** are distinguished

from ones less than the threshold. Much like nanopores are distinguished by the size of the dark spot in the human eye, the average thresholding function judges whether a pixel is a nanopore by its surrounding pixels. The final function, selection, completes two tasks. First, it uses a built-in OpenCV function *findContours*[111] that identifies all contours in the image (in this case, black spots left by the average thresholding function). If the contour surrounds a region greater than a specific ***area*** and is sufficiently circular—as in, it can be surrounded by a bounding box where one side is no longer than three times the other—, the contour is qualified as a nanopore.

In this series of three functions, there are four parameters to tune, as indicated in the bolded words above, with the specific function containing the parameter indicated in parentheses: *grid* (CLAHE), *radius* (Average Thresholding), *threshold* (Average Thresholding), and *area* (Selection). The units of *grid*, *radius*, and *area* are pixels, pixels, and pixels^2, respectively, where one pixel is around 0.4 Å wide in our test images, varying with the magnification of the image. The units of *threshold* are relative but vary from a range of 0 to 255, where 0 indicates black and 255 indicates white. **Figure 2** exhibits the functions in greater detail and specifies the purposes of each parameter (*grid*, *radius*, *threshold*, *area*), with the assistance of line scans that plot pixel intensity versus position across the line scan.

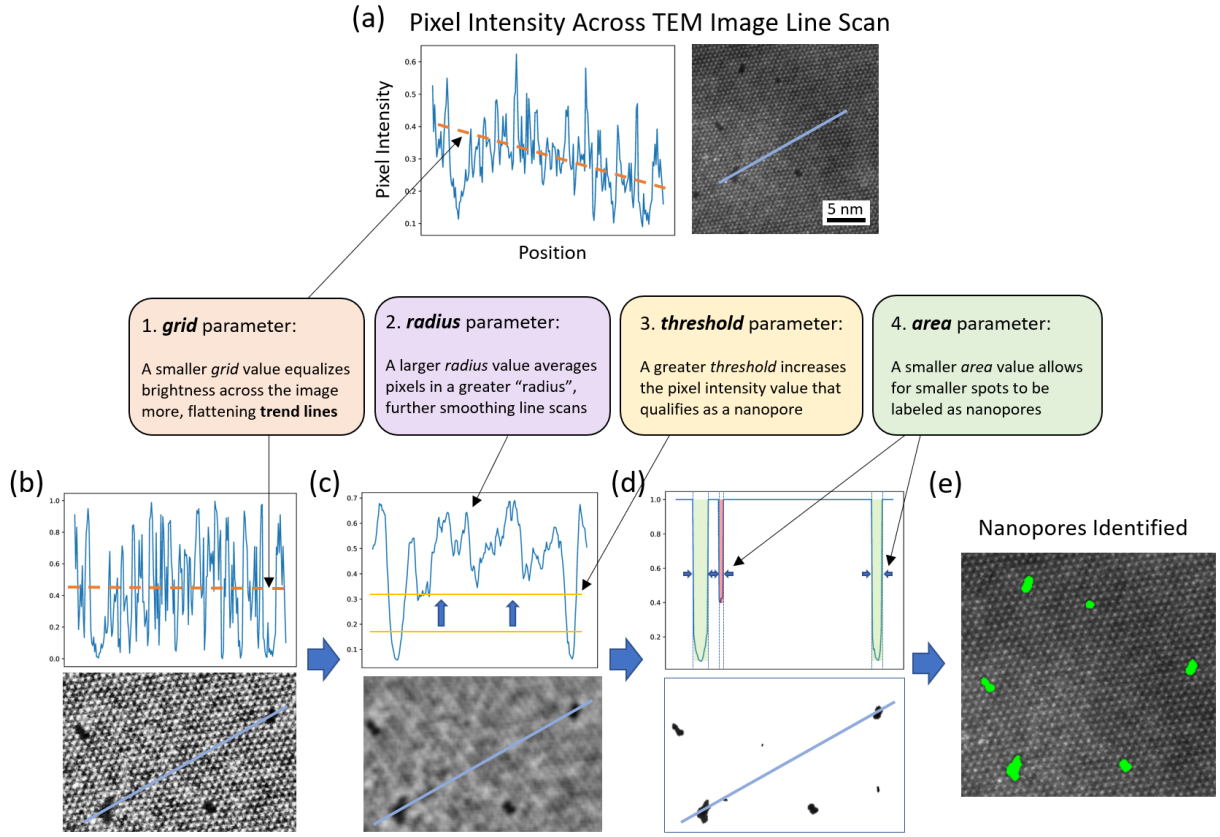

Figure 2. The four parameters (*grid*, *radius*, *threshold*, and *area*) are explained in detail using line scans that plot pixel brightness versus position across the line. (a) The line scan across the original image has varying brightness, resulting in a skewed trendline, which is addressed by (b) a CLAHE function that normalizes each portion independently. (c) The radius parameter smooths the line scan, and the threshold parameter separates darker pixels. d) Dark spots larger than a certain area are separated and (e) identified as nanopores (shown in green in (e)).

Together, these four parameters may be tuned to identify nanopores properly in any TEM image of 2D materials, as long as the pores are distinguishable by eye. Pores can be single atom vacancies up to the size of each grid denoted by the *grid* parameter, which at a minimum is $1/16^{th}$ of the full image. In the images of 2D WS_2 used in our experiments, single W vacancies are recognized by the algorithm, but chalcogen sites (that produce a weaker contrast) are not distinguishable due to contamination of the 2D membrane from the polymer transfer. Provided that the sequence of functions is chosen accurately enough and that checks to normalize for measurable deviations (for example, brightness and magnification) between images are precise, there will likely be a *subset of overlapping parameters* between images that successfully identify all nanopores, provided sufficiently similar images (say, TEM images of the same material, processed the same way and taken with the same microscope settings). To identify the best parameters, this problem was approached with two methods: a brute force grid search with an added visual component which we call *Comprehensive Variable Visual Plotting* (CVVP) which covers all possible parameter combinations, and a gradient ascent method that traverses the parameter space instead encompassing it. First, we discuss our goodness of fit criteria.

2.4 Choosing a goodness of fit criteria

In machine learning, goodness of fit is measured by a user-defined "loss function" that leads an algorithm to reach the most accurate solution. As an example, a common loss function used in computer vision and machine learning is the "hamming distance" between the manually labeled features and the predicted features (that is, the number of positions at which corresponding values are different). In **Figure 3a** below, we focus on a single nanopore, with the left image as the manually labeled "standard" nanopore and the right image as the automatically detected nanopore. In the automatic detection, the green pixels are rightly identified (also known as the true positives, 54 pixels in this example). The red pixels are incorrectly identified (also known as the false positives, 5 pixels in this example). Lastly, the green outlined pixels are unidentified (also known as the false negatives, 11 pixels in this example). The hamming distance is then $5 + 11 = 16$. In our practical case as discussed further in *Section 3.2*, *precision* is a metric which is more suited to our needs due to the focus on minimizing the number of false positive detections. Precision is the fraction of pixels properly detected (true positives) in the number of total pixels proposed (true positives plus false positives), so in the case in **Figure 3a**, $54 / 59 = 91.5\,\%$. **Figure 3b** represents varying precision values across different combinations of the threshold and radius parameters, discussed in the gradient ascent parameter optimization approach in *Section 2.6*. The optimal parameter combination (indicated by the red dot in **Figure 3b**) represents the set of parameters corresponding to the maximum precision.

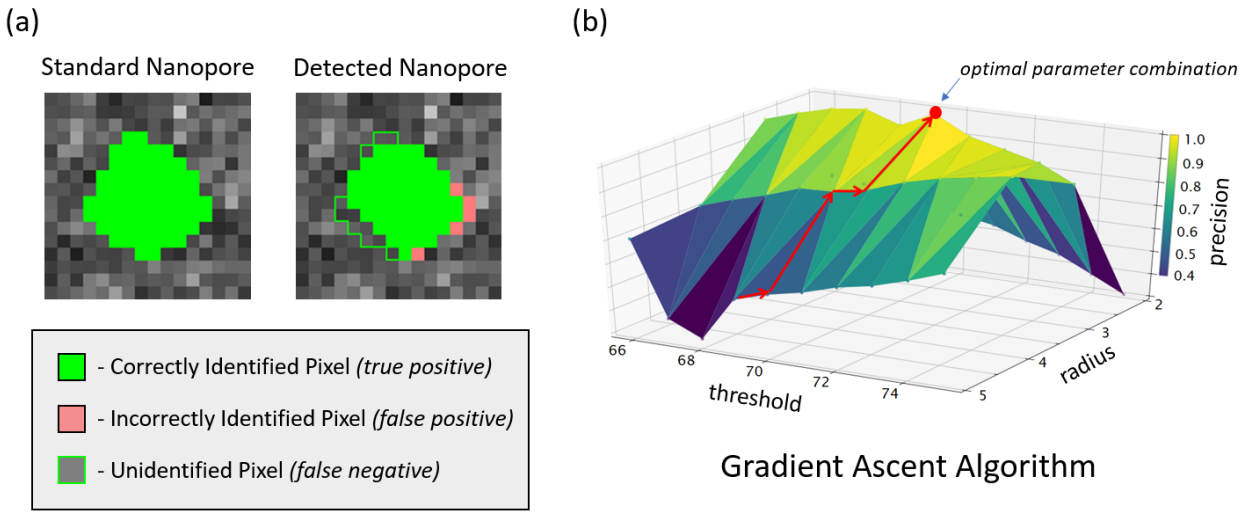

Figure 3. (a) A single nanopore detected and compared with a manually labeled "standard," with the legend underneath indicating which pixels are true positives, false positives, and false negatives. (b) Gradient ascent approach maximizing precision across the threshold and area parameters, where the red arrows demonstrate the direction of the steepest gradient along the precision function. The red point indicates the optimal parameter combination in this example where *threshold* = 71 and *radius* = 3.

2.5 Grid search method via Comprehensive Variable Visual Plotting

Now, given an identification method, we describe the methods for parameter refinement, introducing a variation on the traditional grid search called CVVP where each training standard is considered separately. Steps for a brute force automatic grid search through CVVP are described below.

1. Establish the sequence of computer vision functions (each with their own set of unique parameters) to detect nanopores in TEM images, making sure to normalize images for any variation, such as brightness and magnification.
2. Apply the sequence of computer vision functions to detect nanopores (whether correctly or incorrectly) with all possible combinations of the algorithm's parameters (in our case, *grid*, *radius*, *threshold*, *area*) for a select number of test images (in our case, five), as demonstrated in **Figure 4a**. A larger sampling size will better ensure that the full dataset is properly represented by the sample set, but will come at the cost of run-time, which scales linearly with the number of sample images. If the chosen sample set already properly represents the full dataset, increasing the sampling will not increase the accuracy of detection. Decreasing the sampling size to a certain point will harm the accuracy of the detection methods due to potentially unrepresentative parameters. We have found that 4-5 sample images are sufficient to represent our datasets.
3. Using manually labeled images as "ground truths", calculate the precision for each automatically detected image. Images with precision greater than 90% are deemed successful. Record the successful parameter combinations. Any effect of noise and contamination in the images is automatically considered by the algorithm according to how

the ground truth images are labeled. Furthermore, the CLAHE function ensures that each section of the image is managed separately, allowing for vacancies to be normalized and separated against surrounding noise and contamination.

4. Plot the successful parameter values for each test TEM image together for visual comparison, where each training image is shown in its own color. Choose the combination of parameters that successfully identifies nanopores for all test images (represented by a maximum overlap of colors as illustrated in **Figure 5**).

Considering each sample image separately via CVVP as opposed to a singular loss function across all images is essential in confirming the fit of the computer vision algorithm to the sample images. If there is minimal parameter combination overlap between the sample images, the computer vision algorithm must be altered to fit the problem and address differences between the images, which is especially important in a hard-coded algorithm. Furthermore, the parameter combination with the greatest aggregate score is not necessarily the combination that identifies pores most effectively for the set of sample images (and consequently the full dataset) because one sample image may contribute a much greater score than another. Observing parameter overlap allows for a parameter combination that successfully identifies pores for the *greatest number* of sample, and therefore dataset, images. This brute force approach requires performing N^4 operations of fitting across the detection algorithm (CLAHE, Average Thresholding, and Contour Selection), where N is the number of values for each parameter defined by our parameter space, and 4 is the dimensionality of our parameter space (for our parameters: *grid*, *radius*, *threshold*, and *area*).

In STEM images, the precise and correct experimental focus condition can play an important role and easily blur images. Focus variations shifted from Scherzer-Focus may create over- or under-focused areas that affect the detection of pores. In our methods, over- or under-focus will affect pore recognition only to the extent that it can influence how effectively manually-labeled standards can be created by the user. The CLAHE function further ensures that each segment of the image is managed separately, reducing the effect of focus variations across the image. Overall, focus variations create minimal issue according to this method due to the active role of the scientist in defining the standard data.

2.6 Gradient descent/ascent method

The above CVVP grid search in the parameter space can be greatly optimized using a method usually used in the machine learning, gradient descent/ascent[112]. In simple terms, we initialize our current parameters by starting with a random point of the parameter space and exploring the parameter space in the direction which gives us the greatest increase in precision (where the prediction is closest to the ground truth label). This method can find a quasi-optimal solution in $\mathrm{O}(\mathrm{N})$ computing time (linear) – in our case around 10-15 steps (i.e. 1000 times faster than the full grid space exploration). We note that more modern algorithms exist (such as conjugate gradient methods[113]) but we chose gradient ascent as having the best trade-off between performance and simplicity. Note: usually in machine learning gradient descent is run on a loss function and finds the minima. In our case, we run the gradient method on precision to find the maxima, so the proper name for this variant of gradient descent is "gradient ascent" in our application. Conversely, we may flip the precision function and define the loss function as $\mathrm{loss} = 1 - \mathrm{precision}$.

We can more easily explain this in a 2-parameter space (let's say if the only parameters were threshold and radius), shown in **Figure 3b**. While the grid search will compute the precision for all parameter combinations within the space, gradient descent will follow the path shown by the red line to reach the optimum solution, where the algorithm chooses the direction of the steepest gradient of the precision function.

3. RESULTS:

3.1 Computer vision algorithm parameters and training standards

Table 1 indicates the four (4) parameters refined in the grid search and gradient descent methods, the specific function step with the parameter it is associated with, the range and step size of each parameter value tested, and a few relevant terms.

Table 1. Parameters Altered in CVVP†, Range of Values Tested, and Terminology Used

Parameter Name	Function Step	Range of Values Tested
grid	CLAHE‡	5 - 30, steps of 5
radius	Average Thresholding	0 - 4, steps of 1
threshold	Average Thresholding	40 - 120, steps of 10
area	Selection	0 - 90, steps of 10

*OpenCV = open source computer vision library used in this methodology
†CVVP = "comprehensive variable visual plotting," created to optimize parameters for identification
‡CLAHE = contrast limited adaptive histogram equalization to equalize pixel intensity across an image

TEM images A, B, C, D, and E are a set of five samples of WS_2 with nanopores drilled sporadically throughout by ion irradiation. **Figure 4a** displays these five raw training images in the top row. Underneath, the same images with manually identified nanopores are used as the training images. With the resultant computer vision algorithm developed through the training images and explained later in the rest of *Section 3*, **Figure 4b** displays a few example test images (F, J, I) with nanopores automatically identified and their associated precision metrics. **Figure 4c** shows the resultant detection using the briefly discussed deep learning Mask R-CNN method. **Figure 4d** shows the algorithm applied to BF-STEM images, including the initial contrast reversal that allows for the pores to be detected.

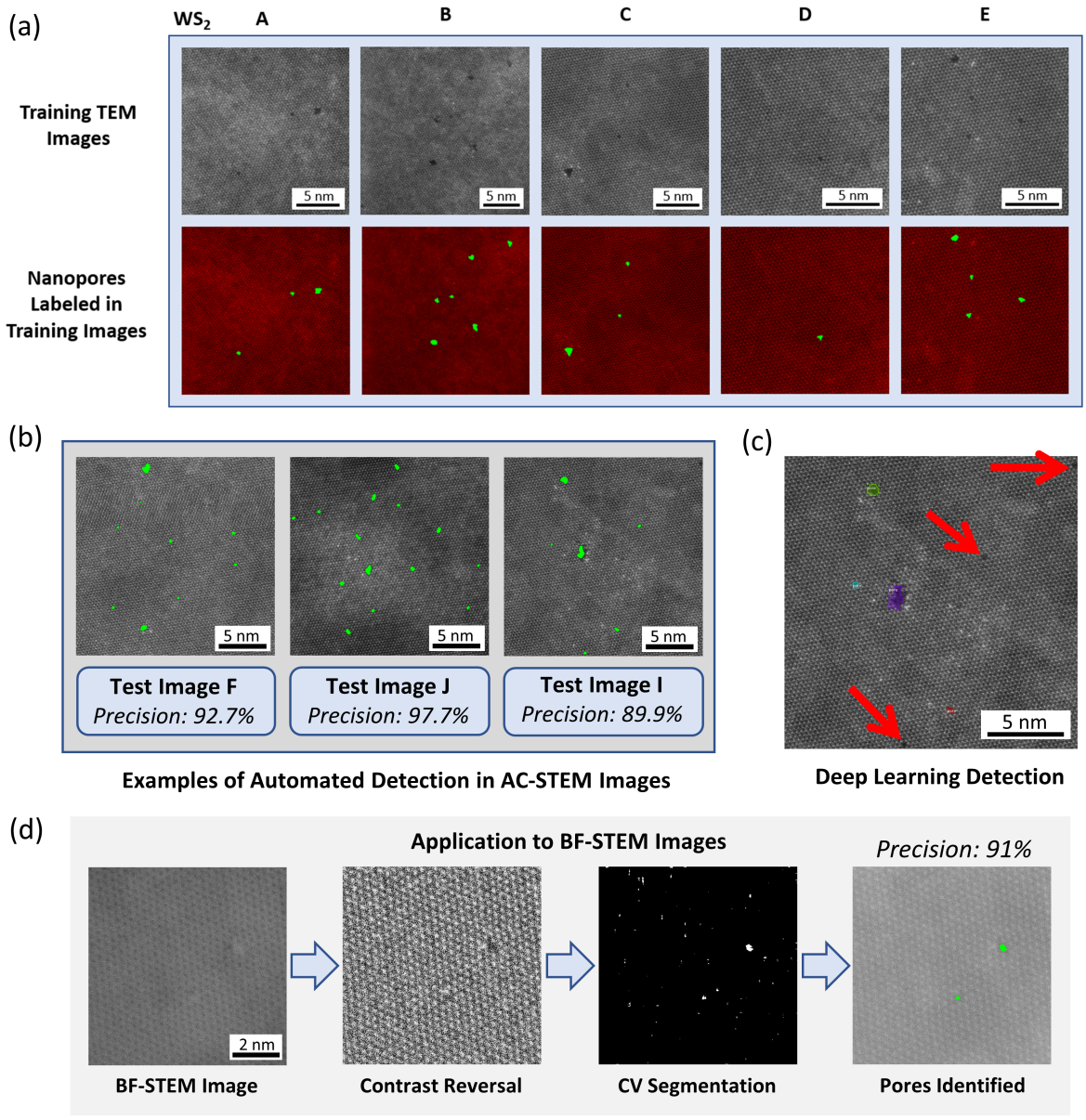

Figure 4. (a) Top row: AC-STEM images (A to E) of ion irradiated 2D WS_2 flake containing nanopores (dark regions in the images). Bottom row: the nanopores are manually identified in bright green for training data. Note the scale bars (5 nm) are varying from A to E, which is accounted for in the identification algorithm by normalizing for magnification. (b) Three example test images with nanopores automatically identified using the computer vision algorithm, with precision metrics indicated. (c) Nanopores from Image I identified using a deep learning Mask R-CNN approach discussed in the text. Some of the pores (indicated by red arrows) are undetected (these include nanopores with small and weak contrast and pores close to the border), as explained in *Section 3.3*. (d) Application of computer vision algorithm to BF-STEM images, which requires a contrast reversal before segmentation. Resultant precision was 91%.

3.2 Results of the CVVP grid search method

Provided the sequence of functions outlined in **Figure 2** and the methods section, as well as the parameters chosen (after some trial-and-error) in **Table I**, there were 2,700 combinations in total of the four parameters for each of the five images provided (6 *grid* x 5 *radius* x 9 *threshold* x 10 *area* = 2,700 unique combinations) in the grid search. Therefore, a total of 13,500 images were generated indicating nanopores (whether accurate or not) across the image. Every image was subsequently compared with the corresponding standard image using the precision metric, where precision greater than 90% was deemed successful. Images with successful parameter combinations were plotted on a graphic representing four dimensions—that is, a two-dimensional grid of two-dimensional plots (see below in **Figure 5**). Overall, the image generation and evaluation required approximately 30 minutes of processing time on an Ubuntu 20.04 Desktop with a 4.2 GHz Intel Core i7-7700K and 64 GB memory.

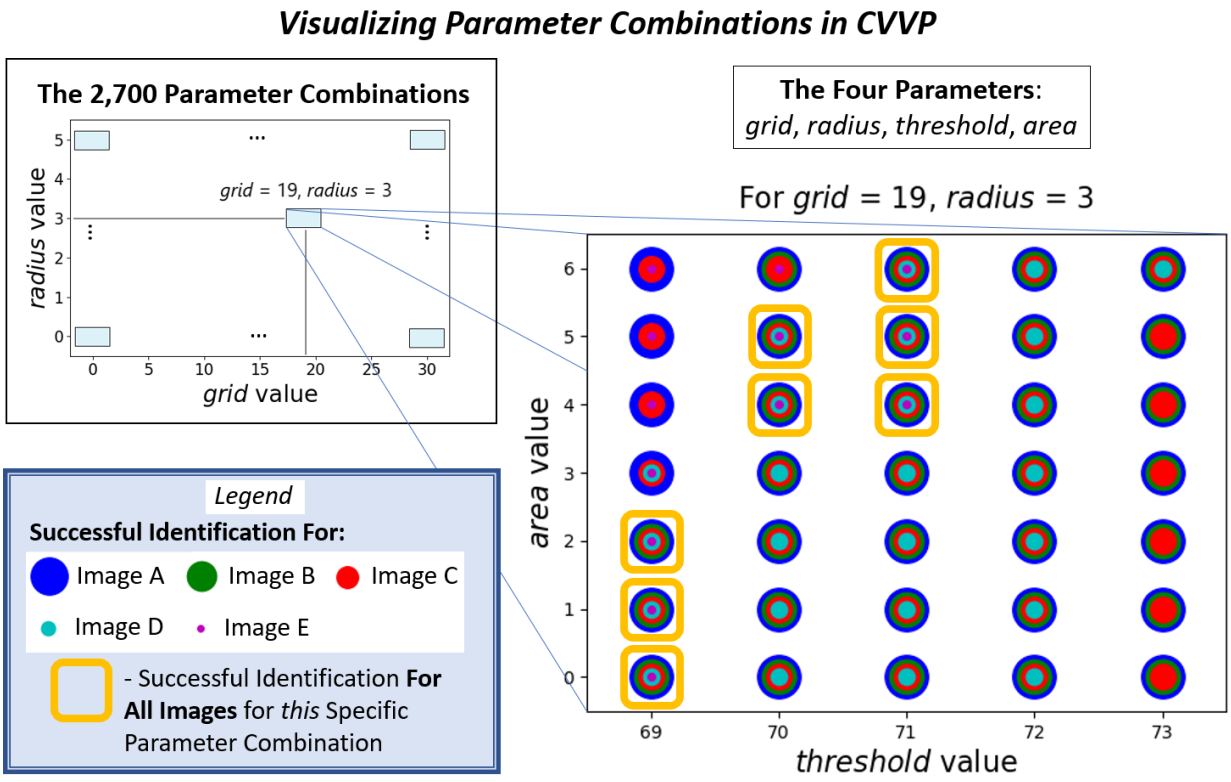

Figure 5. Resulting CVVP plot demonstrating nanopore identification successes for training TEM images A, B, C, D, and E over the four altered parameters (*grid*, *radius*, *threshold*, *area*), with parameter ranges indicated in **Table I**. As an example, for a pair of grid and radius values (grid = 19, radius = 3) from the grid-radius two-parameter space (top left), we show the zoom into the two-parameter subspace for the area and threshold values (bottom right). If a particular pair of area-threshold values identifies the nanopores in a specific image, we mark that parameter pair with a color circle in the graph on the bottom right. The five different color circles represent the successful identification of nanopores within the five TEM images (A to E), as shown in the legend bottom left. Overlapping color circles (two or more) in the area-threshold plot then mean that for these parameters we obtained a successful identification of nanopores simultaneously for two or more TEM images. When all five color circles are present, this means that nanopores in all images have properly been identified. We highlight these successful nanopore identifications in yellow squares.

By analyzing each plot created, the *grid* = 19, *radius* = 3, *threshold* = 71, and *area* = 5 parameter combination is one of the sets that is successful for all five test images, indicating success. To gauge the effectiveness of this method, we use six additional test images and the precision metric, which is often used in machine learning algorithms and defined as $\text{precision} = (\text{number of true positives}) / (\text{number of predicted true values})$ While both precision and recall (which denotes the fraction of positives in the example set)[114] are important in feature recognition, precision is considered the main focus in our case of nanopore detection because we hope to minimize the number of false positives, as in, our goal is to identify true nanopores as accurately as possible and obtain the most accurate number of pores. Given the starting implementation of this method, our intention is to ensure that automatically identified pores are properly selected first before incorrect pores become identified. Recall on the other hand does not consider if a nanopore is incorrectly identified when one is not present. The loss function can be replaced with any success metric as necessary by the user. When run on the test images with the parameter combination found above, we achieved 93.6%, 98.8%, 100%, 100%, and 97.9% precision values for Images A, B, C, D, and E, respectively. When the algorithm was run on an additional 6 test images (F, G, H, I, J, and K) of 2D WS_2 taken under similar environmental conditions, the precision values were 92.7%, 90.4%, 92.0%, 89.9%, 97.7%, and 100%. A few of these example test images with nanopores automatically identified are shown in **Figure 4b**. Across all images, recall had an average value of 64.8%, meaning 64.8% of the surface of the nanopores was included in the detection (usually the detection was missing parts of the nanopore border).

3.3 Results of the gradient ascent (GA) method

Gradient descent/ascent (GD/GA) finds the local minima/maxima for concave functions. However, by adding randomness to its search to ensure the search does not get stuck in a local minimum/maximum, GD/GA can be applied for almost any function. **Figure 3b** illustrates how gradient ascent works to find the maximum. For visualization, we plot the precisions *vs.* threshold and radius for our computer vision algorithm on our training set when the grid and radius parameters are fixed. While the grid-search algorithm would explore all the points on the surface, the GA algorithm will explore only the path shown by the red arrows. We ran the GA and obtained the same optimal parameter combination of *grid* = 19, *radius* = 3, *threshold* = 71, *area* = 5 as with grid search, as expected.

The gradient ascent method proved much more efficient than the grid search method. The relevant parameter space was traversed and the optimal parameter combination found in 10 to 15 steps on average. The run-time in our case was about 1 second on a Core i7 @ 4GHz, which is 2000 times faster than the grid search implementation. (Note: the improvement factor between gradient ascent and grid search scales exponentially with the number of parameters to optimize or the expansion of the parameter grid.)

Although GA was much faster than a brute force grid search, the implementation of a single loss function in GA across all images (as opposed to viewing the parameter successes on each individual image separately as in CVVP) does lead to less insight into how to improve the computer vision algorithm. That is, the visual overlap of parameter combinations in different images in CVVP (rather than all of them averaged together) was useful on our end to choose whether to add or remove a certain parameter or shift the range of values tested, as discussed further in *Section 4*. Thus, gradient ascent is best applied once the computer vision algorithm is confirmed to be effective.

3.3 Application to BF STEM and HRTEM images

In addition to AC-STEM images, the nanopore identification was successfully applied to BF-STEM images, requiring a simple contrast reversal prior to processing. Any concerns about extending the process to ABF imaging (requiring a contrast reversal) should be similarly satisfied according to the analysis of BF-STEM images. Figure 4d is a sample BF-STEM image of porous WS_2 with nanopores automatically identified through the algorithm. However, since the recognition is, at the core, dependent on real-space thresholding, in our HRTEM images it was challenging to identify the pores with this method due to the lack of sufficient contrast difference between pores and lattice.

3.4 Future directions including deep learning methods

We briefly explored how a deep learning method compares to our standard computer vision approach. We chose an instance segmentation architecture (it identifies objects and their shape), which is at the same time state-of the art and also accessible and well-supported—Mask R-CNN.[115] . We slightly customize this architecture (backbone similar to Resnet18, hyperparameters adapted for small features, 2 classes-output, pore and background—see code in Git) starting from an open-source version, matterport_maskrcnn_2017[116], implemented in TensorFlow[117]. To partially alleviate the issue of having a small training set, we performed image augmentation (flip, mirror, rotations, brightness) and transfer learning[118], training the network initially on the COCO (Common Objects in Context) image dataset[119] and then re-training the last layers (the heads of the network) on our nanopore dataset.

For completeness, we briefly comment that in our incipient tests with Mask R-CNN, the training was poor given that we have images for only ~ 50 pores and the results average (as small data sets are common in new experiments). We were able to detect about 50% of the pores, although the contours were less accurate than in the standard computer vision method presented. Examples of detection on Image A using Mask R-CNN are found in **Figure 4c**. We notice that we have trouble detecting small pores and pores with weak contrast, as mentioned in the original paper[115]. Also, pores on the border of the images tend to go undetected, probably as an artifact of how the algorithm applies convolution on the border of the images. The training of the model takes 4 to 12 hours on an RTX 2060 and the detection around 300 to 1000 milliseconds per image. The accuracy can be improved with a larger database and if the models are tuned for this specific application (black and white images, small object sizes). Other architectures [90,102,103] with smaller backbones may give better results for this problem and justify a subsequent study more focused on deep learning methods for nanopore identification.

Ultimately the goal of deep learning for nanopore TEM image analysis will be the development of unified, comprehensive models (trained on images gathered on an extensive variety of materials and TEMs) able to detect and characterize nanopores on every material and TEM model without any training or customization.

4. DISCUSSION

The grid search and gradient ascent methods resulted in the set of parameters best suited to identify nanopores in all images of 2D WS_2 derived from the training images, provided the manually written algorithm (in our case, through OpenCV). Despite the simplicity of standard computer vision methods, or perhaps due to it, there are obvious drawbacks in computer vision applications in general, compared to other methods. First, the sequence of functions applied to each image must be defined manually by the researcher to properly extract the desired features with minimal error. This condition requires a knowledge of computer vision libraries as well as time and effort to develop the most accurate methods. Lacking a proper sequence forfeits any possibility to identify any features or discover a set of function parameters that may work for experimental images. Furthermore, a resultant algorithm works

only to the extent of the images encompassed by the training standards used. For example, if a set of parameters with an algorithm is found to identify nanopores in WS_2 TEM images, the same set of parameters may not work for MoS_2 TEM images. It should be noted, however, that in certain cases where an algorithm may be created accurately, manual development may allow for the inclusion of important expert factors as is sometimes the case in the medical field[120].

Between the grid search and gradient ascent methods, gradient ascent has obvious advantages. Run-time is most distinct, where gradient ascent can deduce the optimal set of parameters thousands of times faster than a grid search can. Computer memory is also an important factor, where the current grid search method through CVVP saves every image created and often requires gigabytes of storage. However, grid search through CVVP has its advantages over gradient ascent. A grid search is comprehensive, which means certainty that the best parameter combination is found, whereas gradient ascent may lead to a parameter combination that is a local rather than global minimum in the loss function. Additionally, visual insight into the grid search is helpful when first developing a computer vision algorithm. If a sequence of functions is first proposed but does not lead to overlap between training images, the positions of successful parameter combinations in the CVVP plot may be used to infer changes to the algorithm, including incorporating more steps or parameters. When developing a new algorithm using standard computer vision methods and optimizing parameters, in the case that there are no parameter successes between all test images, the following steps can be taken:

1. Refining the computer vision algorithm steps to more effectively separate nanopores from the pristine 2D sheet. For example, observing the parameter overlaps in CVVP and deducing trends that may be associated with specific image attributes (examples include magnification and median brightness) that may be incorporated into the algorithm.
2. Introducing a greater selection of parameters for greater flexibility.
3. Operating on a greater number of test images to ensure that one of the training images is not an outlier.
4. There is the possibility that the lack of parameter overlaps can be attributed to the inhomogeneity of the sample images used, in which these methods are not applicable, or higher quality and more consistent images must be used.

Compared to the FFT approach outlined in Ref. 102, standard computer vision methods (including ours) are less easily extended to HRTEM images due to the lack of strong contrast between pores and surrounding lattice, whereas the FFT method recognizes pores from lattice interruptions and a contrast difference is not necessary. At the same time, however, any deviations in the image (including blurring, noise, or contamination) may likely conflict with pore recognition through FFT, and the separation of steps in the computer vision algorithm can allow for simpler troubleshooting. Compared to more recent machine learning methods, the standard computer vision approach has several advantages. Whereas machine learning solutions often require tens of thousands of training images, the bottom-up coding approach allows for a few test cases to effectively represent a much greater set of images, as seen in the efficacy of the standard computer vision methods and the insufficiency in the machine learning methods used. Overall, this results in a simpler process setting up data, and in the case of supervised machine learning, does not require manual labeling of thousands of training data images. Similarly, many machine learning methods require extensive training time, often requiring anything from a few hours to multiple days to produce a model. Though considerable time must be put into algorithm creation in the standard computer vision approach, given a working algorithm, standard computer vision methods are significantly more efficient, as shown in the run times indicated. Furthermore, traditional programming, as a

straightforward, logical approach to solving problems from the bottom up, is typically simpler to troubleshoot, whereas other methods are less decipherable. For example, methods pertaining to machine learning must be checked for overfitting, and care must be taken in proper error analysis to avoid the misinterpretation of results and poor reproducibility. However, we acknowledge that deep learning methods can have a considerable advantage if a large database of nanopore images can be gathered on different materials and TEMs. In the case that a general model can be trained, automated detection without regard to varying material, TEM model, and pore shape would be an ultimate goal. The added functionality of characterization where pores would be classified by shape using this neural network would accelerate TEM technology greatly.

Implementation of the standard computer vision and parameter optimization methods can result in a streamlined method built directly into TEM analysis. A scientist can simply capture a few images of a new nanomaterial, manually label the nanopores in these first images, run one of the parameter optimization methods to obtain the ideal set of parameters, and subsequently identify nanopores in multiple thousands of additional images fully automatically. Furthermore, one may create a database of nanomaterials each with its ideal set of parameters that will allow for successful nanopore identification for any material. For example, WS_2 would be categorized with (*grid* = 19, *radius* = 3, *threshold* = 71, *area* = 5), whereas another material, say $MoSe_2$, may be listed with (*grid* = 10, *radius* = 2, *threshold* = 60, and *area* = 17), allowing for instant automated identification for new TEM images, including real-time recognition in videos or other media. Furthermore, additional tools can be built upon the existing framework to simplify the TEM analysis process. For example, with a nanopore-identified TEM image, a script can output a list of all nanopore locations, sizes, and dimensions. Thus, a plot of the physical distribution of nanopores across a full nanomaterial sample (for example, a micron by micron 2D MoS_2 sample that has been irradiated with a FIB) can be generated for further analysis and applications. These insights can be used for cross-validation with experimental data: nanopore area calculations using identified images can be compared with ionic measurements to confirm theories about ionic transport, atomic electron transport models can be checked with experimental electronic measurements, the mechanical properties of a 2D sheet can be tested with different nanopore patterns, and much more.

5. CONCLUSION:

We presented 2D nanoporous, monolayer membranes and discussed simultaneous TEM observation, fabrication, and analysis. We discussed applications of 2D nanopores with developments in AC-TEM. We delved into methods involving automated TEM image analysis and the advantages and disadvantages of each method. To analyze TEM images of 2D membranes, we developed an algorithm according to standard computer vision approaches through OpenCV, as well as a variation on the grid search that implements a visual component and an implementation of the gradient descent/ascent method for parameter optimization, and then we discussed the implications of each method. We briefly commented on the deep learning method for comparison, although it fails here due to a small data set. Using manually nanopore-identified TEM images of 2D WS_2 as training data, we demonstrated successful nanopore identification in other images using the computer vision approach and parameter refinement, obtaining an average precision of 98% on the training set and 94% on the test set. Lastly, we discussed the implications of TEM image analysis and automated nanopore detection, and proposed a streamlined method built directly into TEM analysis methods, as well as further steps to pursue given an automated nanopore detection program. The juxtaposition of nanomaterial physics, TEM, and images analysis via computer science offers insight into a bright future of microscopy and nanofabrication that will benefit from cross-disciplinary efforts.

Code Availability:

The code developed in this paper, including the CVVP grid search and gradient ascent methods, is openly available at https://github.com/joshualchen/nanopore-identification. Further details regarding OpenCV can be found at https://opencv.org/.

Author Information:

Corresponding Author. *Email: drndic@physics.upenn.edu
Author Contributions. J.C, J.P.T, and M.D conceived the project and implementation idea. J.P.T and P.M.D grew 2D materials, and P.M.D conducted AC-STEM work to retrieve images. J.C wrote all code pertaining to computer vision and CVVP, and A.B implemented gradient ascent and deep learning methods and wrote the pertaining methods and results. J.C and M.D wrote a majority of the paper. All authors have given approval to the final version of the manuscript.
Notes. The authors declare no competing financial interest.

Acknowledgements:

This work was funded by the Rachleff Scholars Program at the University of Pennsylvania School of Engineering and Applied Sciences, by the NSF through the University of Pennsylvania Materials Research Science and Engineering Center (MRSEC) DMR-1720530, as well as NSF Grants EFRI 2-DARE 1542707, NSF DMR 1905045, NSF CCMI Advanced Manufacturing (AM) grant 2002477, and National Institute of Health grant NIH R21 HG010536. We thank Boyan Penkov and Jay Horwath for guidance in setting up systems for remote work, and Dr. Robert Keyse from Lehigh University for assistance with AC-STEM imaging. The AC-STEM images of 2D materials analyzed in this work were obtained using electron microscopes JEOL JEM-ARM200CF S/TEM at the Center for Advanced Materials and Nanotechnology at Lehigh University, and JEOL NEOARM S/TEM with similar beam conditions at the University of Pennsylvania's Singh Center for Nanotechnology. This work was carried out in part at the Singh Center for Nanotechnology, which is supported by the NSF National Nanotechnology Coordinated Infrastructure Program under grant NNCI-1542153. We also acknowledge that the TEM facilities and instrumentation at the University of Pennsylvania are supported by the NSF through the University of Pennsylvania Materials Research Science and Engineering Center (DMR-1720530).

References:

ADDIN ZOTERO_BIBL {"uncited":[],"omitted":[],"custom":[]} CSL_BIBLIOGRAPHY (1) Jiang, Y.; Chen, Z.; Han, Y.; Deb, P.; Gao, H.; Xie, S.; Purohit, P.; Tate, M. W.; Park, J.; Gruner, S. M.; Elser, V.; Muller, D. A. Electron Ptychography of 2D Materials to Deep Sub-Ångström Resolution. *Nature* **2018**, *559* (7714), 343−349. https://doi.org/10.1038/s41586-018-0298-5.

(2) Avsar, A.; Ochoa, H. Colloquium: Spintronics in Graphene and Other Two-Dimensional Materials. *Rev. Mod. Phys.* **2020**, *92* (2), 28.

(3) Zhu, L.; Farhat, M.; Salama, K. N.; Chen, P.-Y. 2 - Two-Dimensional Materials-Based Radio Frequency Wireless Communication and Sensing Systems for Internet-of-Things Applications. In *Emerging 2D Materials and Devices for the Internet of Things*; Tao, L., Akinwande, D., Eds.; Micro and Nano Technologies; Elsevier, 2020; pp 29−57. https://doi.org/10.1016/B978-0-12-818386-1.00002-3.

(4) Luo, C.; Wang, C.; Wu, X.; Zhang, J.; Chu, J. In Situ Transmission Electron Microscopy Characterization and Manipulation of Two-Dimensional Layered Materials beyond Graphene.

Small **2017**, *13* (35), 1604259. https://doi.org/10.1002/smll.201604259.
(5) Meyer, J. C.; Kurasch, S.; Park, H. J.; Skakalova, V.; Künzel, D.; Groß, A.; Chuvilin, A.; Algara-Siller, G.; Roth, S.; Iwasaki, T.; Starke, U.; Smet, J. H.; Kaiser, U. Experimental Analysis of Charge Redistribution Due to Chemical Bonding by High-Resolution Transmission Electron Microscopy. *Nature Materials* **2011**, *10* (3), 209–215. https://doi.org/10.1038/nmat2941.
(6) Meyer, J. C.; Kisielowski, C.; Erni, R.; Rossell, M. D.; Crommie, M. F.; Zettl, A. Direct Imaging of Lattice Atoms and Topological Defects in Graphene Membranes. *Nano Lett.* **2008**, *8* (11), 3582–3586. https://doi.org/10.1021/nl801386m.
(7) He, X.; Xu, T.; Xu, X.; Zeng, Y.; Xu, J.; Sun, L.; Wang, C.; Xing, H.; Wu, B.; Lu, A.; Liu, D.; Chen, X.; Chu, J. In Situ Atom Scale Visualization of Domain Wall Dynamics in VO 2 Insulator-Metal Phase Transition. *Scientific Reports* **2014**, *4* (1), 6544. https://doi.org/10.1038/srep06544.
(8) Nagao, K.; Inuzuka, T.; Nishimoto, K.; Edagawa, K. Experimental Observation of Quasicrystal Growth. *Phys. Rev. Lett.* **2015**, *115* (7), 075501. https://doi.org/10.1103/PhysRevLett.115.075501.
(9) Li, X.; Cheng, S.; Deng, S.; Wei, X.; Zhu, J.; Chen, Q. Direct Observation of the Layer-by-Layer Growth of ZnO Nanopillar by In Situ High Resolution Transmission Electron Microscopy. *Scientific Reports* **2017**, *7* (1), 40911. https://doi.org/10.1038/srep40911.
(10) Schneider, S.; Surrey, A.; Pohl, D.; Schultz, L.; Rellinghaus, B. Atomic Surface Diffusion on Pt Nanoparticles Quantified by High-Resolution Transmission Electron Microscopy. *Micron* **2014**, *63*, 52–56. https://doi.org/10.1016/j.micron.2013.12.011.
(11) Hussaini, Z.; Lin, P. A.; Natarajan, B.; Zhu, W.; Sharma, R. Determination of Atomic Positions from Time Resolved High Resolution Transmission Electron Microscopy Images. *Ultramicroscopy* **2018**, *186*, 139–145. https://doi.org/10.1016/j.ultramic.2017.12.018.
(12) Fischbein, M. D.; Drndić, M. Sub-10 Nm Device Fabrication in a Transmission Electron Microscope. *Nano Letters* **2007**, *7* (5), 1329–1337. https://doi.org/10.1021/nl0703626.
(13) Fischbein, M. D.; Drndić, M. Electron Beam Nanosculpting of Suspended Graphene Sheets. *Appl. Phys. Lett.* **2008**, *93* (11), 113107. https://doi.org/10.1063/1.2980518.
(14) Dyck, O.; Ziatdinov, M.; Lingerfelt, D. B.; Unocic, R. R.; Hudak, B. M.; Lupini, A. R.; Jesse, S.; Kalinin, S. V. Atom-by-Atom Fabrication with Electron Beams. *Nature Reviews Materials* **2019**, *4* (7), 497–507. https://doi.org/10.1038/s41578-019-0118-z.
(15) Lu, Y.; Merchant, C. A.; Drndić, M.; Johnson, A. T. C. In-Situ Electronic Characterization of Graphene Nanoconstrictions Fabricated in a Transmission Electron Microscope. *Nano Lett.* **2011**, *11* (12), 5184–5188. https://doi.org/10.1021/nl2023756.
(16) Puster, M.; Rodríguez-Manzo, J. A.; Balan, A.; Drndić, M. Toward Sensitive Graphene Nanoribbon–Nanopore Devices by Preventing Electron Beam-Induced Damage. *ACS Nano* **2013**, *7* (12), 11283–11289. https://doi.org/10.1021/nn405112m.
(17) Qi, Z. J.; Daniels, C.; Hong, S. J.; Park, Y. W.; Meunier, V.; Drndić, M.; Johnson, A. T. C. Electronic Transport of Recrystallized Freestanding Graphene Nanoribbons. *ACS Nano* **2015**, *9* (4), 3510–3520. https://doi.org/10.1021/nn507452g.
(18) Qi, Z. J.; Rodríguez-Manzo, J. A.; Botello-Méndez, A. R.; Hong, S. J.; Stach, E. A.; Park, Y. W.; Charlier, J.-C.; Drndić, M.; Johnson, A. T. C. Correlating Atomic Structure and Transport in Suspended Graphene Nanoribbons. *Nano Lett.* **2014**, *14* (8), 4238–4244. https://doi.org/10.1021/nl501872x.
(19) Rodríguez-Manzo, J. A.; Qi, Z. J.; Crook, A.; Ahn, J.-H.; Johnson, A. T. C.; Drndić, M. In Situ Transmission Electron Microscopy Modulation of Transport in Graphene Nanoribbons. *ACS Nano* **2016**, *10* (4), 4004–4010. https://doi.org/10.1021/acsnano.6b01419.
(20) Masih Das, P.; Drndić, M. In Situ 2D MoS2 Field-Effect Transistors with an Electron Beam Gate. *ACS Nano* **2020**, *14* (6), 7389–7397. https://doi.org/10.1021/acsnano.0c02908.

(21) Masih Das, P.; Thiruraman, J. P.; Chou, Y.-C.; Danda, G.; Drndić, M. Centimeter-Scale Nanoporous 2D Membranes and Ion Transport: Porous MoS<sub>2<sub> Monolayers in a Few-Layer Matrix. *Nano Lett.* **2019**, *19* (1), 392−399. https://doi.org/10.1021/acs.nanolett.8b04155.
(22) Waugh, M.; Briggs, K.; Gunn, D.; Gibeault, M.; King, S.; Ingram, Q.; Jimenez, A. M.; Berryman, S.; Lomovtsev, D.; Andrzejewski, L.; Tabard-Cossa, V. Solid-State Nanopore Fabrication by Automated Controlled Breakdown. *Nat Protoc* **2020**, *15* (1), 122−143. https://doi.org/10.1038/s41596-019-0255-2.
(23) Thiruraman, J. P.; Masih Das, P.; Drndić, M. Irradiation of Transition Metal Dichalcogenides Using a Focused Ion Beam: Controlled Single- Atom Defect Creation. *Adv. Funct. Mater.* **2019**, *29* (52), 1904668. https://doi.org/10.1002/adfm.201904668.
(24) Forsyth, D. *Computer Vision : A Modern Approach /*; Prentice Hall,: Upper Saddle River, N.J. ;, c2003.
(25) Mendes, R. G.; Pang, J.; Bachmatiuk, A.; Ta, H. Q.; Zhao, L.; Gemming, T.; Fu, L.; Liu, Z.; Rümmeli, M. H. Electron-Driven *In Situ* Transmission Electron Microscopy of 2D Transition Metal Dichalcogenides and Their 2D Heterostructures. *ACS Nano* **2019**, *13* (2), 978−995. https://doi.org/10.1021/acsnano.8b08079.
(26) The Rise and Rise of Graphene. *Nature Nanotechnology* **2010**, *5* (11), 755−755. https://doi.org/10.1038/nnano.2010.224.
(27) Mandyam, S. V.; Kim, H. M.; Drndicé, M. Large Area Few-Layer TMD Film Growths and Their Applications. *J. Phys. Mater.* **2020**, *3* (2), 024008. https://doi.org/10.1088/2515-7639/ab82b3.
(28) 2D materials advances: from large scale synthesis and controlled heterostructures to improved characterization techniques, defects and applications - University of Pennsylvania https://upenn.alma.exlibrisgroup.com (accessed Oct 5, 2020).
(29) Thiruraman, J. P.; Masih Das, P.; Drndić, M. Ions and Water Dancing through Atom-Scale Holes: A Perspective toward "Size Zero." *ACS Nano* **2020**, *14* (4), 3736−3746. https://doi.org/10.1021/acsnano.0c01625.
(30) Xue, L.; Yamazaki, H.; Ren, R.; Wanunu, M.; Ivanov, A. P.; Edel, J. B. Solid-State Nanopore Sensors. *Nature Reviews Materials* **2020**, 1−21. https://doi.org/10.1038/s41578-020-0229-6.
(31) ImageJ https://imagej.net/Welcome (accessed Oct 9, 2020).
(32) Drndić, M. Sequencing with Graphene Pores. *Nature Nanotechnology* **2014**, *9* (10), 743−743. https://doi.org/10.1038/nnano.2014.232.
(33) Danda, G.; Drndić, M. Two-Dimensional Nanopores and Nanoporous Membranes for Ion and Molecule Transport. *Current Opinion in Biotechnology* **2019**, *55*, 124−133. https://doi.org/10.1016/j.copbio.2018.09.002.
(34) Komsa, H.-P.; Kotakoski, J.; Kurasch, S.; Lehtinen, O.; Kaiser, U.; Krasheninnikov, A. V. Two-Dimensional Transition Metal Dichalcogenides under Electron Irradiation: Defect Production and Doping. *Phys. Rev. Lett.* **2012**, *109* (3), 035503. https://doi.org/10.1103/PhysRevLett.109.035503.
(35) Parkin, W. M.; Balan, A.; Liang, L.; Das, P. M.; Lamparski, M.; Naylor, C. H.; Rodríguez-Manzo, J. A.; Johnson, A. T. C.; Meunier, V.; Drndić, M. Raman Shifts in Electron-Irradiated Monolayer MoS_2. *ACS Nano* **2016**, *10* (4), 4134−4142. https://doi.org/10.1021/acsnano.5b07388.
(36) Wang, S.; Li, H.; Sawada, H.; Allen, C. S.; Kirkland, A. I.; Grossman, J. C.; Warner, J. H. Atomic Structure and Formation Mechanism of Sub-Nanometer Pores in 2D Monolayer MoS2. *Nanoscale* **2017**, *9* (19), 6417−6426. https://doi.org/10.1039/C7NR01127J.

(37) Komsa, H.-P.; Kurasch, S.; Lehtinen, O.; Kaiser, U.; Krasheninnikov, A. V. From Point to Extended Defects in Two-Dimensional MoS 2 : Evolution of Atomic Structure under Electron Irradiation. *Phys. Rev. B* **2013**, *88* (3), 035301. https://doi.org/10.1103/PhysRevB.88.035301.
(38) Meyer, J. C.; Eder, F.; Kurasch, S.; Skakalova, V.; Kotakoski, J.; Park, H.-J.; Roth, S.; Chuvilin, A.; Eyhusen, S.; Benner, G.; Krasheninnikov, A. V.; Kaiser, U. An Accurate Measurement of Electron Beam Induced Displacement Cross Sections for Single-Layer Graphene. *Phys. Rev. Lett.* **2012**, *108* (19), 196102. https://doi.org/10.1103/PhysRevLett.108.196102.
(39) Mignuzzi, S.; Pollard, A. J.; Bonini, N.; Brennan, B.; Gilmore, I. S.; Pimenta, M. A.; Richards, D.; Roy, D. Effect of Disorder on Raman Scattering of Single-Layer Mo S 2. *Phys. Rev. B* **2015**, *91* (19), 195411. https://doi.org/10.1103/PhysRevB.91.195411.
(40) Thiruraman, J. P.; Fujisawa, K.; Danda, G.; Das, P. M.; Zhang, T.; Bolotsky, A.; Perea-López, N.; Nicolaï, A.; Senet, P.; Terrones, M.; Drndić, M. Angstrom-Size Defect Creation and Ionic Transport through Pores in Single-Layer MoS 2. *Nano Lett.* **2018**, *18* (3), 1651−1659. https://doi.org/10.1021/acs.nanolett.7b04526.
(41) O'Hern, S. C.; Boutilier, M. S. H.; Idrobo, J.-C.; Song, Y.; Kong, J.; Laoui, T.; Atieh, M.; Karnik, R. Selective Ionic Transport through Tunable Subnanometer Pores in Single-Layer Graphene Membranes. *Nano Lett.* **2014**, *14* (3), 1234−1241. https://doi.org/10.1021/nl404118f.
(42) Islam, M. R.; Kang, N.; Bhanu, U.; Paudel, H. P.; Erementchouk, M.; Tetard, L.; Leuenberger, M. N.; Khondaker, S. I. Tuning the Electrical Property via Defect Engineering of Single Layer MoS2 by Oxygen Plasma. *Nanoscale* **2014**, *6* (17), 10033−10039. https://doi.org/10.1039/C4NR02142H.
(43) Jain, T.; Rasera, B. C.; Guerrero, R. J. S.; Boutilier, M. S. H.; O'Hern, S. C.; Idrobo, J.-C.; Karnik, R. Heterogeneous Sub-Continuum Ionic Transport in Statistically Isolated Graphene Nanopores. *Nature Nanotechnology* **2015**, *10* (12), 1053−1057. https://doi.org/10.1038/nnano.2015.222.
(44) Feng, J.; Graf, M.; Liu, K.; Ovchinnikov, D.; Dumcenco, D.; Heiranian, M.; Nandigana, V.; Aluru, N. R.; Kis, A.; Radenovic, A. Single-Layer MoS2 Nanopores as Nanopower Generators. *Nature* **2016**, *536* (7615), 197−200. https://doi.org/10.1038/nature18593.
(45) Heiranian, M.; Farimani, A. B.; Aluru, N. R. Water Desalination with a Single-Layer MoS2 Nanopore. *Nature Communications; London* **2015**, *6*, 8616. https://doi.org/10.1038/ncomms9616.
(46) Suk, M. E.; Aluru, N. R. Ion Transport in Sub-5-Nm Graphene Nanopores. *The Journal of Chemical Physics* **2014**, *140* (8), 084707. https://doi.org/10.1063/1.4866643.
(47) Suk, M. E.; Aluru, N. R. Water Transport through Ultrathin Graphene. *J. Phys. Chem. Lett.* **2010**, *1* (10), 1590−1594. https://doi.org/10.1021/jz100240r.
(48) Merchant, C. A.; Healy, K.; Wanunu, M.; Ray, V.; Peterman, N.; Bartel, J.; Fischbein, M. D.; Venta, K.; Luo, Z.; Johnson, A. T. C.; Drndić, M. DNA Translocation through Graphene Nanopores. *Nano Lett.* **2010**, *10* (8), 2915−2921. https://doi.org/10.1021/nl101046t.
(49) Garaj, S.; Hubbard, W.; Reina, A.; Kong, J.; Branton, D.; Golovchenko, J. A. Graphene as a Subnanometre Trans-Electrode Membrane. *Nature* **2010**, *467* (7312), 190−193. https://doi.org/10.1038/nature09379.
(50) Schneider, G. F.; Kowalczyk, S. W.; Calado, V. E.; Pandraud, G.; Zandbergen, H. W.; Vandersypen, L. M. K.; Dekker, C. DNA Translocation through Graphene Nanopores. *Nano Letters* **2010**, *10* (8), 3163−3167. https://doi.org/10.1021/nl102069z.
(51) Liu, K.; Feng, J.; Kis, A.; Radenovic, A. Atomically Thin Molybdenum Disulfide Nanopores with High Sensitivity for DNA Translocation. *ACS Nano* **2014**, *8* (3), 2504−2511. https://doi.org/10.1021/nn406102h.
(52) Liu, S.; Lu, B.; Zhao, Q.; Li, J.; Gao, T.; Chen, Y.; Zhang, Y.; Liu, Z.; Fan, Z.; Yang, F.; You, L.; Yu, D. Boron Nitride Nanopores: Highly Sensitive DNA Single-Molecule Detectors. *Advanced Materials* **2013**, *25* (33), 4549−4554. https://doi.org/10.1002/adma.201301336.

(53) Danda, G.; Masih Das, P.; Chou, Y.-C.; Mlack, J. T.; Parkin, W. M.; Naylor, C. H.; Fujisawa, K.; Zhang, T.; Fulton, L. B.; Terrones, M.; Johnson, A. T. C.; Drndić, M. Monolayer WS_2 Nanopores for DNA Translocation with Light-Adjustable Sizes. *ACS Nano* **2017**, *11* (2), 1937−1945. https://doi.org/10.1021/acsnano.6b08028.
(54) Mojtabavi, M.; VahidMohammadi, A.; Liang, W.; Beidaghi, M.; Wanunu, M. Single-Molecule Sensing Using Nanopores in Two-Dimensional Transition Metal Carbide (MXene) Membranes. *ACS Nano* **2019**, *13* (3), 3042−3053. https://doi.org/10.1021/acsnano.8b08017.
(55) Derrington, I. M.; Butler, T. Z.; Collins, M. D.; Manrao, E.; Pavlenok, M.; Niederweis, M.; Gundlach, J. H. Nanopore DNA Sequencing with MspA. *PNAS* **2010**, *107* (37), 16060−16065. https://doi.org/10.1073/pnas.1001831107.
(56) Laszlo, A. H.; Derrington, I. M.; Ross, B. C.; Brinkerhoff, H.; Adey, A.; Nova, I. C.; Craig, J. M.; Langford, K. W.; Samson, J. M.; Daza, R.; Doering, K.; Shendure, J.; Gundlach, J. H. Decoding Long Nanopore Sequencing Reads of Natural DNA. *Nature Biotechnology* **2014**, *32* (8), 829−833. https://doi.org/10.1038/nbt.2950.
(57) Manrao, E. A.; Derrington, I. M.; Laszlo, A. H.; Langford, K. W.; Hopper, M. K.; Gillgren, N.; Pavlenok, M.; Niederweis, M.; Gundlach, J. H. Reading DNA at Single-Nucleotide Resolution with a Mutant MspA Nanopore and Phi29 DNA Polymerase. *Nat Biotechnol* **2012**, *30* (4), 349−353. https://doi.org/10.1038/nbt.2171.
(58) Jain, M.; Koren, S.; Miga, K. H.; Quick, J.; Rand, A. C.; Sasani, T. A.; Tyson, J. R.; Beggs, A. D.; Dilthey, A. T.; Fiddes, I. T.; Malla, S.; Marriott, H.; Nieto, T.; O'Grady, J.; Olsen, H. E.; Pedersen, B. S.; Rhie, A.; Richardson, H.; Quinlan, A. R.; Snutch, T. P.; Tee, L.; Paten, B.; Phillippy, A. M.; Simpson, J. T.; Loman, N. J.; Loose, M. Nanopore Sequencing and Assembly of a Human Genome with Ultra-Long Reads. *Nature Biotechnology* **2018**, *36* (4), 338. https://doi.org/10.1038/nbt.4060.
(59) Feng, J.; Liu, K.; Graf, M.; Dumcenco, D.; Kis, A.; Di Ventra, M.; Radenovic, A. Observation of Ionic Coulomb Blockade in Nanopores. *Nature Mater* **2016**, *15* (8), 850−855. https://doi.org/10.1038/nmat4607.
(60) Hirunpinyopas, W.; Prestat, E.; Worrall, S. D.; Haigh, S. J.; Dryfe, R. A. W.; Bissett, M. A. Desalination and Nanofiltration through Functionalized Laminar MoS_2 Membranes. *ACS Nano* **2017**, *11* (11), 11082−11090. https://doi.org/10.1021/acsnano.7b05124.
(61) Farimani, A. B.; Min, K.; Aluru, N. R. DNA Base Detection Using a Single-Layer MoS2. *ACS Nano* **2014**, *8* (8), 7914−7922. https://doi.org/10.1021/nn5029295.
(62) Zhou, Z.; Hu, Y.; Wang, H.; Xu, Z.; Wang, W.; Bai, X.; Shan, X.; Lu, X. DNA Translocation through Hydrophilic Nanopore in Hexagonal Boron Nitride. *Sci Rep* **2013**, *3* (1), 3287. https://doi.org/10.1038/srep03287.
(63) Masih Das, P.; Danda, G.; Cupo, A.; Parkin, W. M.; Liang, L.; Kharche, N.; Ling, X.; Huang, S.; Dresselhaus, M. S.; Meunier, V.; Drndić, M. Controlled Sculpture of Black Phosphorus Nanoribbons. *ACS Nano* **2016**, *10* (6), 5687−5695. https://doi.org/10.1021/acsnano.6b02435.
(64) Cupo, A.; Masih Das, P.; Chien, C.-C.; Danda, G.; Kharche, N.; Tristant, D.; Drndić, M.; Meunier, V. Periodic Arrays of Phosphorene Nanopores as Antidot Lattices with Tunable Properties. *ACS Nano* **2017**, *11* (7), 7494−7507. https://doi.org/10.1021/acsnano.7b04031.
(65) Thiruraman, J. P.; Masih Das, P.; Drndic, M. Stochastic Ionic Transport in Single Atomic Zero-D Pores. *ACS Nano* **2020**, acsnano.0c04716. https://doi.org/10.1021/acsnano.0c04716.
(66) Pérez, M. D. B.; Nicolaï, A.; Delarue, P.; Meunier, V.; Drndić, M.; Senet, P. Improved Model of Ionic Transport in 2-D MoS_2 Membranes with Sub-5 Nm Pores. *Appl. Phys. Lett.* **2019**, *114* (2), 023107. https://doi.org/10.1063/1.5061825.
(67) Kowalczyk, S. W.; Grosberg, A. Y.; Rabin, Y.; Dekker, C. Modeling the Conductance and DNA Blockade of Solid-State Nanopores. *Nanotechnology* **2011**, *22* (31), 315101. https://doi.org/10.1088/0957-4484/22/31/315101.

(68) Wanunu, M.; Dadosh, T.; Ray, V.; Jin, J.; McReynolds, L.; Drndić, M. Rapid Electronic Detection of Probe-Specific MicroRNAs Using Thin Nanopore Sensors. *Nature Nanotechnology* **2010**, *5* (11), 807−814. https://doi.org/10.1038/nnano.2010.202.
(69) Pennycook, S. J.; Nellist, P. D. *Scanning Transmission Electron Microscopy: Imaging and Analysis*; Springer New York: New York, NY, UNITED STATES, 2011.
(70) Cherns, D. The Surface Structure of (111) Gold Films Sputtered in the High Voltage Electron Microscope A Theoretical Model. *Philosophical Magazine* **1977**, *36* (6), 1429−1444. https://doi.org/10.1080/14786437708238526.
(71) Zhao, X.; Loh, K. P.; Pennycook, S. J. Electron Beam Triggered Single-Atom Dynamics in Two-Dimensional Materials. *J. Phys.: Condens. Matter* **2020**. https://doi.org/10.1088/1361-648X/abbdb9.
(72) Qi, Z. J.; Rodríguez-Manzo, J. A.; Botello-Méndez, A. R.; Hong, S. J.; Stach, E. A.; Park, Y. W.; Charlier, J.-C.; Drndić, M.; Johnson, A. T. C. Correlating Atomic Structure and Transport in Suspended Graphene Nanoribbons. *Nano Lett.* **2014**, *14* (8), 4238−4244. https://doi.org/10.1021/nl501872x.
(73) Puster, M.; Balan, A.; Rodríguez-Manzo, J. A.; Danda, G.; Ahn, J.-H.; Parkin, W.; Drndić, M. Cross-Talk Between Ionic and Nanoribbon Current Signals in Graphene Nanoribbon-Nanopore Sensors for Single-Molecule Detection. *Small* **2015**, *11* (47), 6309−6316. https://doi.org/10.1002/smll.201502134.
(74) Chenna, S.; Crozier, P. A. Operando Transmission Electron Microscopy: A Technique for Detection of Catalysis Using Electron Energy-Loss Spectroscopy in the Transmission Electron Microscope. *ACS Catal.* **2012**, *2* (11), 2395−2402. https://doi.org/10.1021/cs3004853.
(75) Feng, J.; Liu, K.; Graf, M.; Lihter, M.; Bulushev, R. D.; Dumcenco, D.; Alexander, D. T. L.; Krasnozhon, D.; Vuletic, T.; Kis, A.; Radenovic, A. Electrochemical Reaction in Single Layer MoS_2 : Nanopores Opened Atom by Atom. *Nano Lett.* **2015**, *15* (5), 3431−3438. https://doi.org/10.1021/acs.nanolett.5b00768.
(76) Wu, J.; Shan, H.; Chen, W.; Gu, X.; Tao, P.; Song, C.; Shang, W.; Deng, T. In Situ Environmental TEM in Imaging Gas and Liquid Phase Chemical Reactions for Materials Research. *Adv. Mater.* **2016**, *28* (44), 9686−9712. https://doi.org/10.1002/adma.201602519.
(77) Xie, P.; Xiong, Q.; Fang, Y.; Qing, Q.; Lieber, C. M. Local Electrical Potential Detection of DNA by Nanowire−Nanopore Sensors. *Nature Nanotechnology* **2012**, *7* (2), 119−125. https://doi.org/10.1038/nnano.2011.217.
(78) Heerema, S. J.; Vicarelli, L.; Pud, S.; Schouten, R. N.; Zandbergen, H. W.; Dekker, C. Probing DNA Translocations with Inplane Current Signals in a Graphene Nanoribbon with a Nanopore. *ACS Nano* **2018**, *12* (3), 2623−2633. https://doi.org/10.1021/acsnano.7b08635.
(79) Graf, M.; Liu, K.; Sarathy, A.; Leburton, J.-P.; Radenovic, A. Transverse Detection of DNA in a MoS2 Nanopore. *Biophysical Journal* **2018**, *114* (3, Supplement 1), 180a. https://doi.org/10.1016/j.bpj.2017.11.1005.
(80) Traversi, F.; Raillon, C.; Benameur, S. M.; Liu, K.; Khlybov, S.; Tosun, M.; Krasnozhon, D.; Kis, A.; Radenovic, A. Detecting the Translocation of DNA through a Nanopore Using Graphene Nanoribbons. *Nature Nanotechnology* **2013**, *8* (12), 939−945. https://doi.org/10.1038/nnano.2013.240.
(81) Parkin, W. M.; Drndić, M. Signal and Noise in FET-Nanopore Devices. *ACS Sens.* **2018**, *3* (2), 313−319. https://doi.org/10.1021/acssensors.7b00708.
(82) Healy, K.; Ray, V.; Willis, L. J.; Peterman, N.; Bartel, J.; Drndić, M. Fabrication and Characterization of Nanopores with Insulated Transverse Nanoelectrodes for DNA Sensing in Salt Solution. *Electrophoresis* **2012**, *33* (23), 3488−3496. https://doi.org/10.1002/elps.201200350.

(83) Fischbein, M. D.; Drndić, M. Nanogaps by Direct Lithography for High-Resolution Imaging and Electronic Characterization of Nanostructures. *Appl. Phys. Lett.* **2006**, *88* (6), 063116. https://doi.org/10.1063/1.2172292.
(84) Nanopore Integrated Nanogaps for DNA Detection | Nano Letters https://pubs-acs-org.proxy.library.upenn.edu/doi/10.1021/nl403849g (accessed Oct 8, 2020).
(85) Postma, H. W. Ch. Rapid Sequencing of Individual DNA Molecules in Graphene Nanogaps. *Nano Lett.* **2010**, *10* (2), 420−425. https://doi.org/10.1021/nl9029237.
(86) Ivanov, A. P.; Instuli, E.; McGilvery, C. M.; Baldwin, G.; McComb, D. W.; Albrecht, T.; Edel, J. B. DNA Tunneling Detector Embedded in a Nanopore. *Nano Lett.* **2011**, *11* (1), 279−285. https://doi.org/10.1021/nl103873a.
(87) Jin, C.; Lan, H.; Peng, L.; Suenaga, K.; Iijima, S. Deriving Carbon Atomic Chains from Graphene. *Phys. Rev. Lett.* **2009**, *102* (20), 205501. https://doi.org/10.1103/PhysRevLett.102.205501.
(88) The Vast Potential of Atomic-Scale Microscopy https://www.scientificamerican.com/custom-media/biggest-questions-in-science/the-vast-potential-of-atomic-scale-microscopy/ (accessed Oct 9, 2020).
(89) Jesse, S.; Chi, M.; Belianinov, A.; Beekman, C.; Kalinin, S. V.; Borisevich, A. Y.; Lupini, A. R. Big Data Analytics for Scanning Transmission Electron Microscopy Ptychography. *Scientific Reports* **2016**, *6* (1), 26348. https://doi.org/10.1038/srep26348.
(90) Madsen, J.; Liu, P.; Kling, J.; Wagner, J. B.; Hansen, T. W.; Winther, O.; Schiøtz, J. A Deep Learning Approach to Identify Local Structures in Atomic-Resolution Transmission Electron Microscopy Images. *Advanced Theory and Simulations* **2018**, *1* (8), 1800037. https://doi.org/10.1002/adts.201800037.
(91) Horwath, J. P.; Zakharov, D. N.; Megret, R.; Stach, E. A. Understanding Important Features of Deep Learning Models for Transmission Electron Microscopy Image Segmentation. *arXiv:1912.06077 [cond-mat]* **2019**.
(92) Ovchinnikov, O. S.; O'Hara, A.; Jesse, S.; Hudak, B. M.; Yang, S.; Lupini, A. R.; Chisholm, M. F.; Zhou, W.; Kalinin, S. V.; Borisevich, A. Y.; Pantelides, S. T. Detection of Defects in Atomic-Resolution Images of Materials Using Cycle Analysis. *Advanced Structural and Chemical Imaging* **2020**, *6* (1), 3. https://doi.org/10.1186/s40679-020-00070-x.
(93) Ziatdinov, M.; Jesse, S.; Sumpter, B. G.; Kalinin, S. V.; Dyck, O. Tracking Atomic Structure Evolution during Directed Electron Beam Induced Si-Atom Motion in Graphene via Deep Machine Learning. *Nanotechnology* **2020**. https://doi.org/10.1088/1361-6528/abb8a6.
(94) Rosenfeld, A. Computer Vision: Basic Principles. *Proceedings of the IEEE* **1988**, *76* (8), 863−868. https://doi.org/10.1109/5.5961.
(95) Direct measurement of local lattice distortions in strained layer structures by HREM - ScienceDirect https://www-sciencedirect-com.proxy.library.upenn.edu/science/article/pii/030439919390234O?via%3Dihub (accessed Oct 9, 2020).
(96) Galindo, P. L.; Kret, S.; Sanchez, A. M.; Laval, J.-Y.; Yáñez, A.; Pizarro, J.; Guerrero, E.; Ben, T.; Molina, S. I. The Peak Pairs Algorithm for Strain Mapping from HRTEM Images. *Ultramicroscopy* **2007**, *107* (12), 1186−1193. https://doi.org/10.1016/j.ultramic.2007.01.019.
(97) Zuo, J.-M.; Shah, A. B.; Kim, H.; Meng, Y.; Gao, W.; Rouviére, J.-L. Lattice and Strain Analysis of Atomic Resolution Z-Contrast Images Based on Template Matching. *Ultramicroscopy* **2014**, *136*, 50−60. https://doi.org/10.1016/j.ultramic.2013.07.018.
(98) Kramberger, C.; Mittelberger, A.; Hofer, C.; Meyer, J. C. Analysis of Point Defects in Graphene Using Low Dose Scanning Transmission Electron Microscopy Imaging and Maximum Likelihood Reconstruction. *physica status solidi (b)* **2017**, *254* (11), 1700176. https://doi.org/10.1002/pssb.201700176.

(99) Fukushima, K.; Miyake, S.; Ito, T. Neocognitron: A Neural Network Model for a Mechanism of Visual Pattern Recognition. *IEEE Transactions on Systems, Man, and Cybernetics* **1983**, *SMC-13* (5), 826–834. https://doi.org/10.1109/TSMC.1983.6313076.
(100) LeCun, Y.; Boser, B.; Denker, J. S.; Henderson, D.; Howard, R. E.; Hubbard, W.; Jackel, L. D. Backpropagation Applied to Handwritten Zip Code Recognition. *Neural Computation* **1989**, *1* (4), 541–551. https://doi.org/10.1162/neco.1989.1.4.541.
(101) Horwath, J. P.; Zakharov, D. N.; Mégret, R.; Stach, E. A. Understanding Important Features of Deep Learning Models for Segmentation of High-Resolution Transmission Electron Microscopy Images. *npj Computational Materials* **2020**, *6* (1), 1–9. https://doi.org/10.1038/s41524-020-00363-x.
(102) Zhu, Y.; Ouyang, Q.; Mao, Y. A Deep Convolutional Neural Network Approach to Single-Particle Recognition in Cryo-Electron Microscopy. *BMC Bioinformatics* **2017**, *18* (1), 1–10. https://doi.org/10.1186/s12859-017-1757-y.
(103) Maksov, A.; Dyck, O.; Wang, K.; Xiao, K.; Geohegan, D. B.; Sumpter, B. G.; Vasudevan, R. K.; Jesse, S.; Kalinin, S. V.; Ziatdinov, M. Deep Learning Analysis of Defect and Phase Evolution during Electron Beam-Induced Transformations in WS 2. *npj Computational Materials* **2019**, *5* (1), 1–8. https://doi.org/10.1038/s41524-019-0152-9.
(104) Ziatdinov, M.; Dyck, O.; Maksov, A.; Li, X.; Sang, X.; Xiao, K.; Unocic, R. R.; Vasudevan, R.; Jesse, S.; Kalinin, S. V. Deep Learning of Atomically Resolved Scanning Transmission Electron Microscopy Images: Chemical Identification and Tracking Local Transformations. *ACS Nano* **2017**, *11* (12), 12742–12752. https://doi.org/10.1021/acsnano.7b07504.
(105) Zhang, C.; Bengio, S.; Hardt, M.; Recht, B.; Vinyals, O. Understanding Deep Learning Requires Rethinking Generalization. *arXiv:1611.03530 [cs]* **2017**.
(106) Wang, Z. Deep Learning for Image Segmentation: Veritable or Overhyped? 11.
(107) Dietterich, T. Overfitting and Undercomputing in Machine Learning. *ACM Comput. Surv.* **1995**, *27* (3), 326–327. https://doi.org/10.1145/212094.212114.
(108) Selvaraju, R. R.; Cogswell, M.; Das, A.; Vedantam, R.; Parikh, D.; Batra, D. Grad-CAM: Visual Explanations From Deep Networks via Gradient-Based Localization. 9.
(109) OpenCV https://opencv.org/ (accessed Oct 20, 2020).
(110) OpenCV: Histograms - 2: Histogram Equalization https://docs.opencv.org/master/d5/daf/tutorial_py_histogram_equalization.html (accessed Oct 9, 2020).
(111) OpenCV: Finding contours in your image https://docs.opencv.org/3.4/df/d0d/tutorial_find_contours.html (accessed Oct 9, 2020).
(112) Ruder, S. An Overview of Gradient Descent Optimization Algorithms. *arXiv:1609.04747 [cs]* **2017**.
(113) Hady, M. M. A.; Younis, M. S. New Parameter of CG-Method with Exact Line Search for Unconstraint Optimization. *Open Access Library Journal* **2020**, *7* (4), 1–8. https://doi.org/10.4236/oalib.1106236.
(114) Koehrsen, W. Beyond Accuracy: Precision and Recall https://towardsdatascience.com/beyond-accuracy-precision-and-recall-3da06bea9f6c (accessed Oct 19, 2020).
(115) [1703.06870] Mask R-CNN https://arxiv.org/abs/1703.06870 (accessed Oct 20, 2020).
(116) GitHub - matterport/Mask_RCNN: Mask R-CNN for object detection and instance segmentation on Keras and TensorFlow https://github.com/matterport/Mask_RCNN (accessed Oct 21, 2020).
(117) TensorFlow https://www.tensorflow.org/ (accessed Oct 20, 2020).
(118) Pratt, L. Y.; Pratt, L. Y.; Hanson, S. J.; Giles, C. L.; Cowan, J. D. Discriminability-Based Transfer between Neural Networks. In *Advances in Neural Information Processing Systems 5*; Morgan Kaufmann, 1993; pp 204–211.

(119) Lin, T.-Y.; Maire, M.; Belongie, S.; Bourdev, L.; Girshick, R.; Hays, J.; Perona, P.; Ramanan, D.; Zitnick, C. L.; Dollár, P. Microsoft COCO: Common Objects in Context. *arXiv:1405.0312 [cs]* **2015**.
(120) Bhanot, G.; Biehl, M.; Villmann, T.; Zuhlke, D. Biomedical Data Analysis in Translational Research: Integration of Expert Knowledge and Interpretable Models. 11.